Title

Scalable macroporous hydrogels enhance stem cell treatment of volumetric muscle loss

Authors

Eugenis, Ioannis

Wu, Di

Hu, Caroline

et al.

Publication Date

2022-11-01

DOI

10.1016/j.biomaterials.2022.121818

Peer reviewed

HHS Public Access

Author manuscript

Biomaterials. Author manuscript; available in PMC 2023 June 15.

Published in final edited form as:

Biomaterials. 2022 November ; 290: 121818. doi:10.1016/j.biomaterials.2022.121818.

Scalable macroporous hydrogels enhance stem cell treatment of volumetric muscle loss

Ioannis Eugenis[a,f], **Di Wu**[b,f], **Caroline Hu**[f], **Gladys Chiang**[f], **Ngan F. Huang**[c,d,f], **Thomas A. Rando**[b,e,f,g,*]

[a]Department of Bioengineering, Stanford University, Stanford, CA, USA

[b]Department of Neurology and Neurological Sciences, Stanford University School of Medicine, Stanford, CA, USA

[c]The Stanford Cardiovascular Institute, Stanford University, Stanford, CA, USA

[d]Department of Cardiothoracic Surgery, Stanford University, Stanford, CA, USA

[e]Paul F. Glenn Center for the Biology of Aging, Stanford University School of Medicine, Stanford, CA, USA

[f]Veterans Affairs Palo Alto Health Care System, Palo Alto, CA, USA

[g]Broad Stem Cell Research Center, UCLA, Los Angeles, CA, USA

Abstract

Volumetric muscle loss (VML), characterized by an irreversible loss of skeletal muscle due to trauma or surgery, is accompanied by severe functional impairment and long-term disability. Tissue engineering strategies combining stem cells and biomaterials hold great promise for skeletal muscle regeneration. However, scaffolds, including decellularized extracellular matrix (dECM), hydrogels, and electrospun fibers, used for VML applications generally lack macroporosity. As a result, the scaffolds used typically delay host cell infiltration, transplanted cell proliferation, and new tissue formation. To overcome these limitations, we engineered a macroporous dECM-methacrylate (dECM-MA) hydrogel, which we will refer to as a dECM-MA sponge, and investigated its therapeutic potential *in vivo*. Our results demonstrate that dECM-MA sponges promoted early cellularization, endothelialization, and establishment of a pro-regenerative immune microenvironment in a mouse VML model. In addition, dECM-MA sponges enhanced

*Corresponding author. Department of Neurology and Neurological Sciences, Stanford University School of Medicine, Stanford, CA, USA., rando@stanford.edu (T.A. Rando).

Credit author statement

Ioannis Eugenis: Conceptualization, Methodology, Investigation, Validation, Formal analysis, Writing – original draft, Writing – review & editing, Visualization, Project administration; **Di Wu**: Methodology, Investigation, Validation, Formal analysis, Writing – review & editing; **Caroline Hu**: Investigation, Validation; **Gladys Chiang**: Investigation, Validation; **Ngan F. Huang**: Methodology, Writing – review & editing, Supervision, Funding acquisition; **Thomas A. Rando**: Conceptualization, Writing – original draft, Writing – review & editing, Supervision, Funding acquisition.

Declaration of competing interest

The authors declare that they have no known competing financial interests or personal relationships that could have appeared to influence the work reported in this paper.

Appendix A. Supplementary data

Supplementary data to this article can be found online at https://doi.org/10.1016/j.biomaterials.2022.121818.

the proliferation of transplanted primary muscle stem cells, muscle tissue regeneration, and functional recovery four weeks after implantation. Finally, we investigated the scale-up potential of our scaffolds using a rat VML model and found that dECM-MA sponges significantly improved transplanted cell proliferation and muscle regeneration compared to conventional dECM scaffolds. Together, these results validate macroporous hydrogels as novel scaffolds for VML treatment and skeletal muscle regeneration.

Keywords

Volumetric muscle loss; Tissue engineering; Scaffold; Macroporosity; Stem cells; Satellite cells; Skeletal muscle

1. Introduction

Volumetric muscle loss (VML), a traumatic injury characterized by an irrecoverable ablation of skeletal muscle, leads to a loss of tissue function and life-long disability [1,2]. In addition, VML induces a chronic inflammatory response, hindering muscle regeneration and promoting fibrosis [3]. Current therapies for VML are limited to scar tissue debridement and autologous muscle transfers [4]. However, these strategies are accompanied by donor site morbidity, necrosis of transplanted muscle, and limited tissue availability [2]. Tissue engineering holds promise for creating new VML therapies and overcoming limitations associated with autologous tissue grafting.

Several tissue engineered therapies, composed of stem cells, scaffolds, and bioactive factors, have been developed for VML [5]. Bioconstructs that tend to yield more complete regeneration generally include three core components - a biomaterial scaffold, myogenic cells, and non-myogenic cells or growth factors [6–8]. Although engineered materials have been explored as scaffolds for VML applications, decellularized ECM (dECM) is the most widely used material due to the abundance of biochemical cues that are known to be critical for muscle regeneration [9–11]. Freshly isolated muscle stem cells (MuSCs; also known as “satellite cells”), the predominant muscle fiber forming cells in skeletal muscle tissue, have demonstrated enhanced regenerative potential when transplanted into a VML defect [12]. Addition of other muscle-residing cells, which support MuSCs during regeneration, has been shown to further enhance the recovery of muscle mass and function [12–14].

Despite the success of previous studies in restoring muscle structure and function in mouse muscle following VML injuries, studies in larger animals have been far less encouraging [13,15,16]. Predominant challenges associated with large defects such as VML include maintaining transplanted cell survival and promoting rapid bioconstruct vascularization to provide nutrients to support regenerating tissue [17,18]. Pre-vascularized bioconstructs have demonstrated anastomosis with host vasculature in VML models, but myofiber regeneration was limited [19,20]. Bioconstructs require immediate and uniform perfusion following transplantation, as diffusion can sustain cells only within a few hundred microns from the liquid-scaffold interface [21,22].

Scaffold porosity is known to promote angiogenesis and regeneration in various tissue applications [23,24]. Macroporosity, and an interconnected pore matrix, are critical for promoting diffusion of nutrients and removal of waste during regeneration [25,26]. In addition, scaffold macroporosity has been shown to improve the survival, proliferation, and differentiation of transplanted stem cells [27,28]. Nonetheless, there are few studies of macroporous scaffolds for VML applications [29, 30]. In fact, most fabrication methods used to produce scaffolds for VML therapies yield microporous, rather than macroporous, bioconstructs [31]. Decellularization protocols affect the mechanical characteristics, including decreasing porosity of the resulting dECM [32]. Other scaffolds used for VML applications, including conventional hydrogels and electrospun fibers, are microporous due to their nanoscale polymer networks [5]. As a result, microporous materials physically constrain encapsulated cells, have limited diffusion with increasing size, and impede cell migration [28].

Here, we engineer a macroporous dECM-methacrylate (dECM-MA) hydrogel, which we will refer to as a dECM-MA sponge, and evaluate its potential to enhance primary muscle stem cell transplantation and tissue regeneration following VML injury. We find that the dECM-MA sponge significantly enhanced the proliferation of MuSCs *in vitro* and *in vivo* compared to conventional dECM scaffold. In addition, dECM-MA sponges demonstrated improved tissue regeneration and muscle function recovery. Moreover, we demonstrate the scale-up potential of the dECM-MA sponge in a larger VML model, namely a rat model. Our findings demonstrate the importance of scaffold macroporosity in tissue engineered therapies for VML.

2. Materials and methods

2.1. Animals

C57BL/6, FVB-Tg (CAG-luc-GFP)L2G85Chco/J, and NSG (NOD.Cg-Prkdc^{scid} Il2rg^{tm1Wjl}/SzJ) male mice were obtained from The Jackson Laboratory. Sprague Dawley and RNU Nude rats were obtained from Charles River. Animals were housed and maintained in the Veterinary Medical Unit at the Veterans Affairs Palo Alto Health Care Systems. Animal protocols were approved by the Institutional Animal Care and Use Committee at the Veterans Affairs Palo Alto Health Care Systems.

2.2. Skeletal muscle decellularization and digestion

Skeletal muscle tissue was decellularized as previously described [33]. Briefly, hindlimb muscles (C57BL/6 mice or Sprague Dawley rats) were dissected and placed in a decellularization buffer (1% SDS, 50 I·U./ml penicillin-streptomycin in PBS) for 4 days with daily buffer changes. The decellularized ECM (dECM) was strained and placed in isopropyl alcohol (IPA) for 2 days to remove lipids that could inhibit subsequent dECM gelation. The dECM was rinsed in UltraPure water for 1 day to remove residual SDS and IPA, frozen, lyophilized, and stored at −20 °C. Purified dECM used for future transplantation was cut into VML defect dimensions prior to lyophilization. Remaining dECM was added to a pepsin solution (1 mg/ml pepsin in 0.1 M HCl) at a concentration of 10 mg dECM/1 ml pepsin solution and stirred at 120 rpm for 2 days at room temperature. The digested dECM

solution was neutralized with 1 M NaOH and dialyzed against UltraPure water for 1 day using 3.5 K MWCO dialysis tubing. The purified solution was lyophilized and stored at −20 °C.

2.3. dECM-MA and GelMA synthesis

Skeletal muscle dECM methacrylate (dECM-MA) was synthesized using a modified protocol as previously described [34]. Purified dECM was dissolved in 0.5 M acetic acid at a concentration of 3.75 mg/ml at 4 °C overnight. The dECM solution was titrated to pH 8–9 using 1 M NaOH. Under continuous stirring, methacrylic anhydride (MA) was added to the solution at a ratio of 621 mg MA to 600 mg dECM and allowed to react for 2 days at 4 °C. The resulting dECM-MA was dialyzed against UltraPure water for 1 week using 3.5 K MWCO dialysis tubing, frozen, and lyophilized. Gelatin methacrylate (GelMA) was synthesized using a modified protocol as previously described [35]. Gelatin was dissolved in PBS at 50 °C to achieve a final concentration of 10% (w/v). Under continuous stirring, MA was added to the gelatin solution at a rate of 0.5 ml/min to achieve 20% MA (v/v) and allowed to react for 1 h at 50 °C. The resulting GelMA solution (~80% degree of functionalization) was diluted 2-fold with warmed PBS, dialyzed against UltraPure water for 1 week using 12–14 kDa MWCO dialysis tubing, frozen, and lyophilized. Dried dECM-MA and GelMA were stored at −20 °C until use.

2.4. Gelatin microsphere fabrication

Gelatin microspheres were fabricated using a water-in-oil emulsion method, as previously described [36]. Briefly, 10% gelatin in PBS was added dropwise to a mixture of mineral oil and 1% Span 80 that had been preheated to 50 °C. The emulsion was stirred at 250 rpm for 10 min and then cooled in an ice bath under continued stirring for an additional 10 min, allowing the gelatin to physically crosslink. The mixture was then diluted 2-fold by cold PBS and vigorously shaken for 1 min. Gelatin microspheres were separated from the oil phase by centrifugation, rinsed four times with PBS, sieved, and stored at 4 °C until use. Microspheres used for imaging were fixed with 4% PFA for 20 min under agitation and rinsed with PBS. Microspheres were then stained by a 1-h incubation with NHS-Fluorescein at room temperature, rinsed, and imaged using a Zeiss LSM 710 confocal microscope. Microsphere diameters were quantified using the “Analyze Particles” command in FIJI software.

2.5. dECM-MA sponge fabrication

dECM-MA and GelMA were dissolved in PBS to achieve final concentrations of 5% and 10%, respectively. Lithium phenyl-2,4,6-trimethylbenzoylphosphinate (LAP) photo-initiator was added to each hydrogel precursor solution at a final concentration of 0.05%. Gelatin microspheres were rinsed with a solution of 2.5% GelMA and 0.05% LAP twice and separated by centrifugation. Rinsed microspheres were resuspended in the dECM-MA hydrogel precursor solution at a 2:1 ratio (microspheres:hydrogel), transferred to silicone molds, and exposed to UV light (365 nm, 4 mW/cm^2) for 5 min. The crosslinked microsphere-hydrogel composites were incubated in PBS at 37 °C for 2 days, changing the PBS daily, to allow the gelatin microspheres to dissolve completely. Sponges used for imaging were fixed with 4% PFA for 20 min and rinsed with PBS. Remaining sponges were

frozen in liquid nitrogen, lyophilized, and stored at −20 °C until use. Hybrid dECM-MA/GelMA sponges were fabricated by mixing the respective hydrogel solutions at different ratios prior to microsphere resuspension and crosslinking. To fabricate polymer-specific labeled sponges, dECM-MA and GelMA hydrogel precursors were labeled with 5 (6)-TAMRA NHS Ester and NHS-Fluorescein, respectively, prior to sponge fabrication.

2.6. Scaffold imaging, reconstruction, and porosity quantification

Fixed dECM and dECM-MA sponge scaffolds were labeled with Alexa Fluor™ 647 NHS Ester and rinsed with PBS. Scaffolds were then incubated in a solution of 100 μg/ml 70,000 MW Fluorescein isothiocyanate-dextran in PBS at room temperature for 1 h. Scaffolds were imaged using a Zeiss LSM 710 confocal microscope and 200-μm Z-stacks were obtained. Z-stacks were imported into IMARIS software to create 3D surface renders of the scaffolds and their void space. Scaffold porosity (void fraction) was quantified as the fraction of the void volume over the total volume of the Z-stack.

2.7. MuSC and MRC purification

MuSCs and muscle resident cells (MRCs) were isolated from mouse skeletal muscle tissue as previously described [12,37]. Muscles were harvested from the hindlimbs of C57BL/6 or FVB-Tg (CAG-luc-GFP) L2G85Chco/J mice, mechanically dissociated, and enzymatically digested for 90 min in a 500 U/ml Collagenase II-Ham's F10 solution at 37 °C. Following centrifugation, the mixture was further digested for 30 min in a Collagenase II (100 U/ml) + Dispase (2 U/ml)-Ham's F10 solution at 37 °C. The resulting cell suspension was filtered, washed with Ham's F10 medium, and stained with CD31-APC, CD45-APC, Sca-1-Pacific Blue, and VCAM-PeCy7 antibodies at 1:100 dilutions for 15 min at 4 °C. Unbound antibodies were washed with Ham's F10 medium and the cell suspension was sorted using calibrated BD-FACS Aria II or BD-FACS Aria III flow cytometers equipped with 488-nm, 633-nm, and 405-nm lasers. MuSCs (CD31−/CD45−/Sca1−/VCAM+), hematopoietic cells (HCs) (CD31−/CD45+/Sca1−/VCAM−), endothelial cells (ECs) (CD31+/CD45−/Sca1+/VCAM−), fibro-adipogenic progenitors (FAPs) (CD31−/CD45−/Sca1+/VCAM−), and fibroblast-like cells (FLCs) (CD31−/CD45−/Sca1−/VCAM−)) were isolated using the gating strategy in Supplementary Fig. 1.

2.8. Bioconstruct preparation

For mouse VML bioconstructs, cell suspensions containing 150,000 MuSCs, 140,000 ECs, 100,000 HCs, 40,000 FAPs, and 70,000 FLCs were seeded onto each scaffold immediately after sorting. Cell seeding ratios were maintained for rat VML bioconstructs, scaling each cell population four-fold - 600,000 MuSCs, 560,000 ECs, 400,000 HCs, 160,000 FAPs, and 280,000 FLCs per bioconstruct. Bioconstructs were incubated for 20 min at 37 °C to allow cells to attach before adding Ham's F10 medium to the wells. Bioconstructs, along with acellular scaffolds, were incubated in Ham's F10 medium overnight at 37 °C until transplantation.

2.9. VML injury and bioconstruct implantation

Animals (3-month-old male NSG mice or 1-month-old male RNU nude rats) were placed under 2.5% isoflurane anesthesia for surgical procedures. Buprenorphine SR (mouse model: 1 mg/kg; rat model: 1.2 mg/kg) and Baytril (5 mg/kg) were administered subcutaneously. An incision was made to the skin, exposing the TA, and Bupivacaine (mouse model: 2 mg/kg; rat model: 8 mg/kg) was administered dropwise onto the muscle. Following a mouse VML model described previously [12], a 40% ablation of the TA muscle was created by removing a 2 mm × 7 mm × 2 mm piece of muscle. For the rat VML model, a 20% ablation of the TA was created by removing a 3 mm × 12 mm × 3 mm piece of muscle. The excised muscles were weighed to ensure consistent ablation between animals in each model (mouse model: 15 mg; rat model: 60 mg). Immediately after muscle ablation, animals were randomized to receive one of the following treatment groups per leg: (1) acellular dECM; (2) acellular dECM-MA sponge; (3) acellular dECM-MA/GelMA sponge; (4) dECM + MuSC/MRCs; (5) dECM-MA sponge + MuSCs/MRCs; (6) dECM-MA/GelMA sponge + MuSCs/MRCs. Hybrid dECM-MA/GelMA sponges were fabricated at a 50:50 ratio of dECM-MA to GelMA to decrease dECM-MA concentration without significantly affecting hydrogel mechanical properties. Following transplantation, scaffolds were secured in place by suturing surrounding muscle and then closing the skin incision with 8–0 sutures. Muscles that received no treatment (VML only controls) were also sutured closed.

2.10. Bioluminescence imaging (BLI)

Animals were anesthetized using 2.5% isoflurane and received an intraperitoneal injection of sterile D-Luciferin (150 mg/kg of body weight). Following injection, animals were transferred to a Xenogen IVIS-Spectrum System for imaging. Every minute, a 5 s exposure image was taken, until the peak bioluminescent signal began to decline. BLI data were analyzed using Living Image Software. Initial MuSC survival on dECM, dECM-MA sponges, and dECM-MA/GelMA sponges was also evaluated by *in vitro* BLI. Ham's F10 medium containing 150 μg/ml D-Luciferin was added to bioconstructs in culture wells and imaged using a Tecan Spark microplate reader. Luminescence was measured every 10 min (at 37 °C) until the maximum signals were detected.

2.11. In vivo muscle functional testing

TA force measurements were performed using an Aurora Scientific 3-in-1 Whole Animal System, as previously described [38,39]. Animals were anesthetized using 2.5% isoflurane and placed on the stage in the supine position. After adjusting the leg to the correct position and securing the foot of the animal against the footplate, the knee joint was stabilized to ensure isometric muscle contractions. Electrodes were placed subcutaneously above the TA muscle until the maximum twitch force was identified. The electrodes were then secured with clamps. Tetanic curves were generated following muscle stimulation at 150 Hz. Electrodes were adjusted as needed to achieve regularly shaped tetanic curves (an uninterrupted, sharp vertical increase at the start of stimulation, followed by a flat plateau, and then a sharp vertical decrease at the end of stimulation). A minimum of 4 tetanic contraction measurements were recorded per treatment group and the peak tetanic force was

selected for downstream analysis. Force measurements of untreated VML and uninjured controls (n = 4) were recorded alongside those of the experimental groups.

2.12. Gait analysis

Video recording and gait analysis were performed using a DigiGait system by Mouse Specifics. Prior to recording, mice were allowed to acclimate in the chamber for 5 min (static treadmill) and then acclimated to the moving treadmill by gradually increasing the belt speed to 20 cm/s over a period of 5 min. Once the treadmill belt was set to 20 cm/s (0-degree incline), the video recording began. Videos were recorded until a minimum of four 5 s clips of uninterrupted running were obtained. DigiGait software was used for video processing, including thresholding binary image sequences to decrease noise and to remove artifacts, and for gait analysis.

2.13. Tissue harvest and histology

TA muscles were dissected, weighed, frozen in optimal cutting temperature medium, and stored at −80 °C until sectioning. Using a Leica CM3050S cryostat, frozen muscles were cut into 10 μm thick sections and mounted on Genesee Scientific charged slides. Sections were fixed for 15 min using 2% PFA, rinsed with PBS, and stored at −20 °C until use. Samples were then stained according to the manufacturer's protocols with Hematoxylin and Eosin (Sigma) and Gomori Trichrome (Richard-Allan Scientific) stains.

2.14. Immunostaining

Tissue sections were permeabilized using 0.5% TritonX-100 in PBS for 20 min at room temperature. To prevent non-specific binding of antibodies, sections were blocked using 10% BSA in PBS for 1 h at room temperature. Primary antibodies were diluted in an antibody buffer solution (0.3% Tween-20 in PBS (PBST), 10% donkey serum), applied to the blocked sections, and allowed to incubate overnight at 4 °C. After three washes of 0.3% PBST, fluorescently labeled secondary antibodies diluted in the antibody buffer were added and incubated for 1 h at room temperature. Samples were washed three times with 0.3% PBST and once with PBS, before being mounted with Vectashield antifade mounting medium. Antibodies, along with their source and dilution, used in this study are as follows: CD31 (Abcam, ab182981, 1:500), CD68 (Invitrogen, FA-11, 1:250), CD206 (Proteintech, 18704–1-AP, 1:250), Laminin (Abcam, ab11576, 1:500), Neurofilament (Invitrogen, MA5–14981, 1:250), Alexa Fluor 594 Donkey anti-Rat (Invitrogen, A21209, 1:500), Alexa Fluor 647 Donkey anti-Rabbit (Invitrogen, A21207, 1:500).

2.15. Imaging and image analysis

Colorimetric stains were imaged using a Keyence BZ-X fluorescence microscope equipped with 2X and 10X air objectives. Immunostained sections were imaged using a Zeiss LSM 710 confocal microscope with a 10X air objective and tile-stitched to view the entire cross-sectional area of each section. FIJI software was used to analyze all images for this study. The polygon tool was used to quantify muscle and scaffold cross-sectional areas. The "Analyze Particles" command was used to quantify the number of nuclei, muscle fiber CSA, and positively stained areas (CD31, CD68, CD206, NF).

2.16. Statistical analysis

GraphPad Prism v9 (GraphPad Software) was used to perform statistical analyses and create graphs. Ordinary one-way ANOVA, including multiple comparison tests, and *t*-tests were used for statistical analysis. All error bars represent S.E.M.

3. Results

Macroporous dECM-MA sponge scaffolds were fabricated using a modified porogen leaching method described previously [40]. After decellularizing and digesting mouse skeletal muscle tissue, we functionalized the resulting dECM with methacrylate groups to yield a photo-crosslinkable dECM-MA hydrogel (Fig. 1A). Next, gelatin microspheres were fabricated using a water-in-oil emulsion and purified to be used as porogens (Fig. 1B). Microspheres were sieved to achieve a uniform size distribution ranging from 75 to 150 μm, with an average diameter of 120 ± 20 μm (Fig. 1C). The dECM-MA hydrogel precursor was mixed with the microspheres and photo-crosslinked to create a composite. Finally, microspheres were dissolved to yield a macroporous dECM-MA sponge scaffold (Fig. 1A). Efficient porogen removal from the sponge scaffold was validated using fluorescently labeled gelatin microspheres (Supplementary Fig. 2). Unlike conventional dECM scaffolds, dECM-MA sponges have a homogenous macropore matrix (Fig. 1D, Supplementary Fig. 3A).

Next, scaffolds were incubated in a solution containing FITC-labeled dextran, with a molecular weight too large to penetrate polymer networks, to visualize their void spaces (Fig. 1E). As expected, dECM-MA sponges are significantly more porous (68 ± 5% porosity) than conventional dECM scaffolds (4.1 ± 0.6% porosity) (Fig. 1F, Supplementary Videos 1,2). Quantified void space volumes of dECM scaffolds were generally attributed to a textured surface, rather than porosity of the bulk scaffold. The macroporous matrix of dECM-MA sponges is highly interconnected, with most pore connection sizes ranging from 20 to 50 μm (Supplementary Figs. 3B and C). In addition, dECM-MA sponges have more surface area for cell attachment than dECM scaffolds (Supplementary Fig. 4).

Supplementary video related to this article can be found at https://doi.org/10.1016/j.biomaterials.2022.121818.

Since the dECM-MA sponge is hydrogel-based, other hydrophilic polymers can be easily incorporated to decrease the amount of dECM needed to produce each scaffold, thus increasing scalability. Gelatin methacrylate (GelMA), a versatile and readily available biomaterial, was mixed with dECM-MA at different ratios before crosslinking to produce a range of dECM-MA/GelMA hybrid sponges. Labeling of each material shows that both polymers were homogeneously distributed throughout the sponge backbone (Fig. 1G).

3.1. Acellular dECM-MA sponges promote early cellularization, endothelialization, and establishment of a pro-regenerative immune microenvironment in a mouse VML model

To investigate the effects of macroporosity on endogenous cell recruitment, vascularization, and immunomodulation, acellular dECM and dECM-MA sponge scaffolds were implanted into a mouse VML defect (Supplementary Fig. 5). Nuclear staining demonstrated that

significantly more host cells were present within dECM-MA sponges than in control dECM scaffolds at both two and four weeks after implantation (Fig. 2A and B). In addition, the distribution of cells within sponge scaffolds was more homogenous than in dECM scaffolds. Immunostaining revealed a population of cells within the scaffolds to be of the vascular endothelium, identified by $CD31^+$ staining (Fig. 2C). Compared to dECM controls, dECM-MA sponges contained significantly more $CD31^+$ cells at both two and four weeks after implantation (Fig. 2D). $CD31^+$ staining within the sponges was also observed farther from the scaffold-muscle interface. Moreover, $CD31^+$cells within dECM-MA sponges were maintained for four weeks after implantation.

VML results in a dysregulated immune response with prolonged inflammation and impaired muscle regeneration [3,41]. Macrophages, which polarize between pro-inflammatory (M1) and pro-regenerative (M2) phenotypes, play a critical role in regulating both the immune microenvironment and myogenesis [42,43]. Staining for CD68 and CD206, M1-and M2-macrophage markers, respectively, revealed differing immune microenvironments between dECM and dECM-MA sponge scaffolds (Fig. 2E). Compared to dECM-MA sponges, dECM scaffolds contained more $CD68^+$ and fewer CD206+ cells at both two and four weeks after implantation (Supplementary Fig. 6). Quantification of the ratio between M2-and M1-macrophages (CD206+/CD68+ cells) in each scaffold demonstrated that dECM-MA sponges promoted an early and sustained pro-regenerative environment whereas dECM scaffolds promoted an increasingly pro-inflammatory environment (Fig. 2F). Overall, these data suggest that dECM-MA sponges promoted early cellularization, endothelialization, and establishment of a pro-regenerative immune microenvironment, unlike control dECM scaffolds.

3.2. Macroporous dECM-MA sponges enhance proliferation of primary MuSCs and regeneration of skeletal muscle in a mouse VML model

After characterizing endogenous responses to the acellular scaffolds, we sought to test whether our macroporous dECM-MA sponges would enhance the proliferation of transplanted cells. First, we isolated luciferase-expressing (Luc+) MuSCs, along with a luciferase-negative (Luc−) population of muscle resident cells (MRCs) previously defined by our lab [12], from mouse skeletal muscle (Supplementary Fig. 1). Next, we seeded the mixed cell population onto dECM and dECM-MA sponge scaffolds (Fig. 3A). Bioconstructs were cultured *in vitro* for three days and luminescence was measured over time to compare MuSC proliferation kinetics. Sponge bioconstructs yielded enhanced MuSC proliferation compared to dECM controls (Fig. 3B). In addition, MuSCs cultured on dECM-MA sponges began proliferating earlier than MuSCs on dECM scaffolds. By day three, luminescence from MuSCs on dECM scaffolds increased 1.25-fold, whereas luminescence from MuSCs on dECM-MA sponges increased 2.49-fold. We then examined MuSC proliferation kinetics *in vivo* by transplanting bioconstructs into mouse VML defects within 14 h of bioconstruct fabrication. We measured bioluminescence over four weeks. As expected, dECM-MA sponges also enhanced MuSC proliferation *in vivo*. Over four weeks, luminescence from MuSCs seeded on dECM control scaffolds and dECM-MA sponges increased by ~10-fold and ~100-fold, respectively (Fig. 3C and D). Together, these results suggest that dECM-MA sponges enhance MuSC proliferation *in vitro* and *in vivo*.

Next, we sought to determine if the improved proliferation of MuSCs on dECM-MA sponges would translate to enhanced muscle regeneration. TA muscles were harvested four weeks after bioconstruct implantation and analyzed to characterize bioconstruct and muscle morphology. Unlike regenerating myofibers in muscles treated with dECM-MA sponges, myofibers surrounding dECM scaffolds were mostly disorganized and irregularly shaped (Fig. 4A). Quantification of cross-sectional area revealed that dECM scaffolds degraded more than dECM-MA sponges (Supplementary Fig. 7). Given the covalent crosslinking of dECM-MA, longer scaffold degradation times are expected relative to dECM controls. Despite differences in scaffold degradation, muscles treated with dECM-MA sponges showed a statistically significant increase in size as measured by cross-sectional area (Fig. 4B). In addition, more regenerating myofibers were observed in muscles treated with dECM-MA sponges compared to those treated with dECM control scaffolds (Fig. 4C).

Restoration of not only muscle structure but also muscle function is critical for successful VML therapy. Four weeks after bioconstruct implantation, we electrically stimulated TA muscles *in vivo* and measured isometric tetanic forces. Muscles treated with dECM-MA sponges showed a ~80% recovery in force production (Fig. 4D). On the other hand, muscles treated with dECM scaffolds did not show a significant improvement in force production compared to untreated VML groups. To further characterize functional muscle regeneration, we conducted gait analysis by tracking the footprints of each mouse as they walked on a transparent treadmill, using the DigiGait system (Fig. 4E). Limbs treated with dECM-MA sponges had a significantly longer stance duration, the time that the paw is in contact with the belt during each step, than untreated limbs (Fig. 4F). Paw placement angles and their variability between steps for both treatment groups were not significantly different than those of uninjured controls (Supplementary Fig. 8). During either walking or running, each stride is made up of a braking (paw deceleration), propulsion (paw acceleration), and swing phase. TA muscles control ankle dorsiflexion and play an important role in maintaining the braking phase of each step [44]. Treatment of TA VML injuries with dECM-MA sponges resulted in longer braking phases, more closely resembling those in uninjured controls (Fig. 4G). Neither stance nor braking phase durations were significantly improved in limbs treated with dECM scaffolds compared to untreated VML controls (Fig. 4F and G).

Vascularization, innervation, and immunomodulation are essential processes for promoting functional skeletal muscle regeneration following VML injury [5]. Immunostaining for CD31 was used to characterize endothelialization within the remaining scaffolds four weeks after bioconstruct implantation. Consistent with our previous findings (Fig. 2), where acellular sponges yielded enhanced scaffold endothelialization *in vivo*, significantly more $CD31^+$ cells were observed within dECM-MA bioconstructs compared to dECM bioconstructs (Fig. 5A and B). To evaluate innervation in each treatment group, we quantified the number of neuromuscular junctions (NMJs) in areas of regenerating muscle fibers. NMJs were distinguished by colocalization of synaptic structures, identified by staining for neurofilaments (NF), and postsynaptic acetylcholine receptor clusters, visualized using fluorescently labeled α-bungarotoxin (αBTX). More NMJs were present in muscles treated with dECM-MA sponges compared to those treated with dECM scaffolds (Fig. 5C and D).

Finally, we characterized macrophage polarization within the bioconstructs four weeks post-implantation by immunostaining for CD68 and CD206, markers for M1-and M2-macrophages, respectively. Similar to our findings within acellular scaffolds implanted *in vivo* (Fig. 2), bioconstructs made of dECM-MA sponges promoted a more pro-regenerative microenvironment than did dECM scaffolds (Supplementary Fig. 9). Although M2-polarized macrophages are known to promote myogenic cell differentiation, excessive M2-activation can promote fibrosis by TGF-β signaling [45]. Since fibrosis impedes muscle regeneration, we evaluated collagen deposition within each scaffold and along their muscle-scaffold interfaces using Trichrome staining. Compared to dECM scaffolds, which had high contents of collagen deposition, dECM-MA sponges contained minimal fibrosis (Supplementary Fig. 10). In addition, the macroporous architecture of the remaining dECM-MA sponges was conserved four weeks after implantation.

3.3. Hybrid dECM-MA/GelMA sponges improve MuSC transplantation and muscle regeneration following VML to a similar extent as dECM-MA sponges

Compared to conventional dECM scaffolds, dECM-MA sponges require less dECM material for fabrication because their volumes are made up of mostly empty space. Since tissue availability limits the scalability of dECM-based scaffolds for large defects, we investigated if a decrease in dECM-MA concentration would affect the therapeutic efficacy of sponge bioconstructs for VML therapy. As described in Fig. 1, we fabricated a variety of sponge compositions with decreasing dECM-MA concentration by incorporating GelMA, a highly biocompatible and relatively inexpensive biomaterial, into the hydrogel backbone of the sponge. We prepared bioconstructs by seeding our defined cell populations on sponges made either entirely of dECM-MA or of a 50:50 ratio of dECM-MA to GelMA. Bioconstructs were transplanted into mouse VML defects and bioluminescence was measured to characterize MuSC proliferation *in vivo*. Four weeks after implantation, luminescence from MuSCs increased by roughly two orders of magnitude when seeded on dECM-MA and dECM-MA/GelMA sponges, with no significant difference between groups (Fig. 6A and B). TA muscles were harvested four weeks after implantation to compare muscle regeneration between the sponge bioconstruct treatments. No significant differences in regenerating myofiber density were observed between muscles treated with dECM-MA and those treated with dECM-MA/GelMA bioconstructs (Fig. 6C and D). Moreover, dECM-MA and dECM-MA/GelMA bioconstructs yielded similar recoveries of muscle size and function (Figure E,F). Taken together, these data suggest that decreasing the concentration of dECM-MA, while incorporating GelMA, does not decrease the therapeutic potential of dECM-MA sponge bioconstructs.

Given this finding, we next investigated if dECM-MA was needed altogether. Using a similar experimental setup, we evaluated the therapeutic potential of dECM-MA/GelMA and GelMA-only sponge bioconstructs in a mouse VML model. Compared to luminescence from MuSCs on GelMA-only sponges, luminescence from MuSCs on dECM-MA/GelMA sponges was significantly higher 28 days after bioconstruct implantation (Supplementary Fig. 11A and B). TA muscles were harvested four weeks after implantation to characterize muscle regeneration between sponge bioconstruct treatments. Significantly more regenerating myofibers were observed in muscles treated with dECM-MA/GelMA

bioconstructs compared to those treated with GelMA-only bioconstructs (Supplementary Fig. 11C and D). There results suggest that addition of dECM-MA to GelMA sponge scaffolds enhances therapeutic potential of this treatment.

3.4. Macroporous dECM-MA sponges improve muscle regeneration and functional recovery in a rat VML model

After demonstrating that scaffold macroporosity significantly enhanced MuSC transplantation and muscle regeneration in a mouse VML model, we sought to investigate the scale-up potential of dECM-MA sponge bioconstructs by using a rat VML model. To prepare the bioconstructs, we isolated Luc + MuSCs and Luc− MRCs from mouse skeletal muscle and seeded them onto dECM and dECM-MA sponge scaffolds. Scaffold volume and cell populations were scaled four-fold; cell seeding ratios were identical to those used for the mouse studies. Bioconstructs were implanted into rat VML defects and bioluminescence was measured to characterize MuSC proliferation *in vivo*. Consistent with our findings using the mouse VML model (Fig. 3), luminescence from MuSCs seeded on dECM-MA sponges increased by ~100-fold over four weeks in the rat VML model (Fig. 7A and B). Four weeks after implantation, TA muscles were harvested to evaluate skeletal muscle regeneration. Compared to treatment with dECM bioconstructs, treatment with dECM-MA sponge bioconstructs yielded a statistically significant increase in muscle size as measured by cross-sectional area (Fig. 7C and D). In addition, more regenerating myofibers were observed in muscles treated with dECM-MA sponges compared to those treated with dECM control scaffolds (Fig. 7C,E). Treatment with dECM-MA sponge bioconstructs also yielded a significant recovery of muscle function, unlike treatment with dECM bioconstructs (Fig. 7F). Together, these results demonstrate that dECM-MA sponges improve MuSC transplantation and skeletal muscle regeneration in a larger injury model, suggesting the possibility of using these bioconstructs as a scalable approach to treat VML.

4. Discussion

VML injury overwhelms the endogenous repair capacity of skeletal muscle, resulting in permanent loss of function and scar tissue formation [2,4]. Although previous studies of stem cell therapy for treating VML have been encouraging, scalability poses a significant obstacle for these strategies. Specifically, sufficient oxygen transport, which becomes challenging in large bioconstructs, is required to sustain cells following implantation [21,46,47]. As a result, maintaining transplanted cell survival and promoting rapid bioconstruct vascularization limit the success of stem cell therapies in large defects such as VML [5]. In this study, we engineer macroporous dECM-MA hydrogels to overcome the limitations associated with scalability of stem cell therapies for treating VML. Scaffold macroporosity was shown to promote early cellularization, endothelialization, and establishment of a pro-regenerative immune microenvironment. In addition, dECM-MA sponges significantly increased MuSC proliferation *in vitro* and in VML models *in vivo.* Macroporous dECM-MA sponges enhanced myofiber regeneration, recovery of muscle function, and tissue reconstruction in mouse and rat VML models compared to conventional dECM scaffolds.

Scaffold macroporosity has been shown to promote angiogenesis and regeneration in various tissue types [23,24]. Here, we found that dECM-MA sponges contained significantly more $CD31^+$ cells than did conventional dECM scaffolds *in vivo*. One limitation of this experiment is that we specifically characterized cells of the vascular endothelium. As such, we conclude that dECM-MA sponges promote endothelialization. However, further characterization is needed to evaluate vascularization, the formation of both the endothelium and smooth muscle layer, as well as anastomosis with host vasculature. Formation of a functional vascular network will play an important role in improving oxygen transport through bioconstructs of larger sizes. In this study, we validate that macroporous dECM-MA sponges support stem cell survival and muscle regeneration in a scaled-up rat VML model. Transplantation of sponge bioconstructs into an even larger defect, such as a porcine or ovine VML model [13,16], will provide insights into the efficacy of this treatment strategy in a wound closer to human-scale.

Since VML results in critically sized defects, scaffolds used for regenerative medicine must be scalable to be clinically translatable. Choice of material as well as scaffold fabrication method are key determinants of bioconstruct translatability. Although dECM is the most widely used scaffold for VML applications, scalability is limited in part by tissue availability. By synthesizing a dECM-MA hydrogel and fabricating sponges with ~70% void space by volume, we significantly reduced the amount of dECM needed to produce each scaffold. The hydrogel-porogen fabrication method used to create the dECM-MA sponges allows for other materials to be easily incorporated, further decreasing the amount of dECM required to produce each scaffold. In this study, we demonstrated that dECM-MA/GelMA sponge scaffolds, made up of equal parts dECM-MA and GelMA, enhanced MuSC transplantation and muscle regeneration comparably to pure dECM-MA sponges. Other engineered scaffolds with mixed compositions that have been used for VML therapy are generally fabricated by electrospinning, which produces micro- and nano-scale fibers that more closely mimic the architecture of native ECM [5]. Despite improved scaffold tunability, electrospinning is complex and has relatively slow production rates, hindering the fabrication of larger scaffolds. In addition, electrospun scaffolds are known to have poor cell infiltration, limited porosity, and low mechanical strength [48]. Here, we illustrate a simple, scalable strategy for fabricating scaffolds designed for large-scale defects, such as VML. Moreover, sponge scaffold properties, including degradation rate, porosity, and mechanical strength, can easily be tuned by modifying the hydrogel or porogen during scaffold fabrication.

3D bioprinting has emerged as a powerful tool for fabricating bioconstructs that mimic the complex, yet organized structure of skeletal muscle tissue [49,50]. Spatial patterning of multiple cell types and biomaterials in a layer-by-layer fashion by 3D bioprinting has already been used to produce bioconstructs for defects at human-scale [51]. Since dECM-MA hydrogels and gelatin microgels have been used as bioinks, separately, the dECM-MA sponge fabrication strategy described in this work is easily translatable for 3D bioprinting [34,52]. Therefore, bioconstructs with more complex, macroporous architectures can be fabricated to further enhance skeletal muscle regeneration following VML. For example, dECM-MA sponges with aligned macropores generated by 3D printing will introduce anisotropy, which is known to enhance myogenesis, vascularization, and innervation of

bioconstructs transplanted into VML models [5,53]. Scaffold pore properties, including size, orientation, and interconnectivity, have been shown to play role in modulating the foreign body response, vascularization, and tissue regeneration [54–57]. Limitations, including low printing speed and resolution, associated with 3D printing must be addressed to realize the full potential of large, 3D-printed bioconstructs [58]. Nonetheless, bioconstructs generated by 3D bioprinting and transplanted into VML defects have demonstrated improved muscle regeneration and tissue architecture [7,59].

We previously demonstrated that dECM bioconstructs, containing MuSCs and MRCs, were able to partially restore the structure and function of muscles with VML injuries [12]. However, the preparation of these bioconstructs was complex. To achieve homogenous cell attachment, MuSCs and MRCs were suspended in a hydrogel and injected into a dECM scaffold at multiple locations using a syringe pump. Since MuSCs began losing viability a few hours after seeding, bioconstructs had to be perfused in a bioreactor for 24 h prior to transplantation. Here, we demonstrate that macroporous dECM-MA scaffolds not only enhanced scalability of bioconstructs containing MuSCs and MRCs, but also significantly simplified bioconstruct preparation. The highly interconnected, macroporous matrix of dECM-MA sponges allowed for cells seeded on the scaffold to distribute uniformly and to attach without being suspended in a hydrogel. In addition, MuSC survival and proliferation *in vivo* were significantly improved in dECM-MA sponges compared to our previously described dECM bioconstructs [12], thus eliminating the need for a bioreactor. Despite the simpler bioconstruct preparation, we observed a further increase in muscle regeneration, as measured by muscle cross-sectional area, and functional recovery in muscles treated with dECM-MA sponges compared to those treated with our previously described bioconstructs [12,60].

5. Conclusion

In summary, we have engineered a macroporous hydrogel scaffold that enhances muscle stem cell transplantation and tissue regeneration, demonstrating the potential of a dECM-MA sponge bioconstruct as a viable treatment for VML. Our findings underscore the importance of scaffold macroporosity in regenerative medicine therapies for large-scale defects such as VML. We demonstrated the scalability of our approach, with respect to scaffold fabrication and regenerative efficacy *in vivo*, using mouse and rat VML models. Future studies could further explore the potential of macroporous hydrogel scaffolds to promote skeletal muscle regeneration in even larger defect models.

Supplementary Material

Refer to Web version on PubMed Central for supplementary material.

Acknowledgements

This work was supported by grants from the Department of Veterans Affairs (Merit Review I01RX001222 and 1I01BX004259–01A1) and the National Science Foundation and Center for the Advancement of Science in Space (1829534) to NFH and the NIH (NIH/NCMRR: P2C HD086843) to TAR. The authors also acknowledge the NSF Graduate Research Fellowship Program (GRFP) for its support to IE. We thank the members of the Rando

laboratory for their support during stem cell isolations and feedback on the work described. Schematics created with BioRender.com.

Data availability

The raw/processed data required to reproduce these findings cannot be shared at this time as the data also forms part of an ongoing study.

References

[1]. Corona BT, Wenke JC, Ward CL, Pathophysiology of volumetric muscle loss injury, Cells Tissues Organs 202 (2016) 180–188, 10.1159/000443925. [PubMed: 27825160]

[2]. Garg K, Ward CL, Hurtgen BJ, Wilken JM, Stinner DJ, Wenke JC, et al. , Volumetric muscle loss: persistent functional deficits beyond frank loss of tissue, J. Orthop. Res. 33 (2015) 40–46, 10.1002/jor.22730. [PubMed: 25231205]

[3]. Larouche J, Greising SM, Corona BT, Aguilar CA, Robust inflammatory and fibrotic signaling following volumetric muscle loss: a barrier to muscle regeneration, Cell Death Dis. 9 (2018) 409, 10.1038/s41419-018-0455-7. [PubMed: 29540673]

[4]. Grogan BF, Hsu JR, Skeletal Trauma Research Consortium, Volumetric muscle loss, J. Am. Acad. Orthop. Surg. 19 (Suppl 1) (2011) S35–S37, 10.5435/00124635-201102001-00007. [PubMed: 21304045]

[5]. Eugenis I, Wu D, Rando TA, Cells, scaffolds, and bioactive factors: engineering strategies for improving regeneration following volumetric muscle loss, Biomaterials 278 (2021), 121173, 10.1016/j.biomaterials.2021.121173. [PubMed: 34619561]

[6]. Nakayama KH, Quarta M, Paine P, Alcazar C, Karakikes I, Garcia V, et al. , Treatment of volumetric muscle loss in mice using nanofibrillar scaffolds enhances vascular organization and integration, Commun. Biol. 2 (2019) 170, 10.1038/s42003-019-0416-4. [PubMed: 31098403]

[7]. Kim JH, Kim I, Seol Y-J, Ko IK, Yoo JJ, Atala A, et al. , Neural cell integration into 3D bioprinted skeletal muscle constructs accelerates restoration of muscle function, Nat. Commun. 11 (2020) 1025, 10.1038/s41467-020-14930-9. [PubMed: 32094341]

[8]. Baker HB, Passipieri JA, Siriwardane M, Ellenburg MD, Vadhavkar M, Bergman CR, et al. , Cell and growth factor-loaded keratin hydrogels for treatment of volumetric muscle loss in a mouse model, Tissue Eng. 23 (2017) 572–584, 10.1089/ten.TEA.2016.0457.

[9]. Sarrafian TL, Bodine SC, Murphy B, Grayson JK, Stover SM, Extracellular matrix scaffolds for treatment of large volume muscle injuries: a review, Vet. Surg. 47 (2018) 524–535, 10.1111/vsu.12787. [PubMed: 29603757]

[10]. Csapo R, Gumpenberger M, Wessner B, Skeletal muscle extracellular matrix - what do we know about its composition, regulation, and physiological roles? A narrative review, Front. Physiol. 11 (2020) 253, 10.3389/fphys.2020.00253. [PubMed: 32265741]

[11]. Brown BN, Badylak SF, Extracellular matrix as an inductive scaffold for functional tissue reconstruction, Transl. Res. 163 (2014) 268–285, 10.1016/j.trsl.2013.11.003. [PubMed: 24291155]

[12]. Quarta M, Cromie M, Chacon R, Blonigan J, Garcia V, Akimenko I, et al. , Bioengineered constructs combined with exercise enhance stem cell-mediated treatment of volumetric muscle loss, Nat. Commun. 8 (2017), 15613, 10.1038/ncomms15613. [PubMed: 28631758]

[13]. Ward CL, Pollot BE, Goldman SM, Greising SM, Wenke JC, Corona BT, Autologous minced muscle grafts improve muscle strength in a porcine model of volumetric muscle loss injury, J. Orthop. Trauma 30 (2016) e396–e403, 10.1097/BOT.0000000000000673. [PubMed: 27466826]

[14]. Corona BT, Garg K, Ward CL, McDaniel JS, Walters TJ, Rathbone CR, Autologous minced muscle grafts: a tissue engineering therapy for the volumetric loss of skeletal muscle, Am. J. Physiol. Cell Physiol. 305 (2013) C761–C775, 10.1152/ajpcell.00189.2013. [PubMed: 23885064]

[15]. Rodriguez BL, Vega-Soto EE, Kennedy CS, Nguyen MH, Cederna PS, Larkin LM, A tissue engineering approach for repairing craniofacial volumetric muscle loss in a sheep following a

2, 4, and 6-month recovery, PLoS One 15 (2020), e0239152, 10.1371/journal.pone.0239152. [PubMed: 32956427]

[16]. Novakova SS, Rodriguez BL, Vega-Soto EE, Nutter GP, Armstrong RE, Macpherson PCD, et al. , Repairing volumetric muscle loss in the ovine peroneus tertius following a 3-month recovery, Tissue Eng. 26 (2020) 837–851, 10.1089/ten.TEA.2019.0288.

[17]. Mertens JP, Sugg KB, Lee JD, Larkin LM, Engineering muscle constructs for the creation of functional engineered musculoskeletal tissue, Regen. Med. 9 (2014) 89–100, 10.2217/rme.13.81. [PubMed: 24351009]

[18]. Grounds MD, Obstacles and challenges for tissue engineering and regenerative medicine: Australian nuances, Clin. Exp. Pharmacol. Physiol. 45 (2018) 390–400, 10.1111/1440-1681.12899. [PubMed: 29193254]

[19]. Gilbert-Honick J, Iyer SR, Somers SM, Lovering RM, Wagner K, Mao H-Q, et al. , Engineering functional and histological regeneration of vascularized skeletal muscle, Biomaterials 164 (2018) 70–79, 10.1016/j.biomaterials.2018.02.006. [PubMed: 29499437]

[20]. Pilia M, McDaniel JS, Guda T, Chen XK, Rhoads RP, Allen RE, et al. , Transplantation and perfusion of microvascular fragments in a rodent model of volumetric muscle loss injury, Eur. Cell. Mater. 28 (2014) 11–23, 10.22203/ecm.v028a02.; discussion 23. [PubMed: 25017641]

[21]. Rouwkema J, Koopman B, Blitterswijk C, Dhert W, Malda J, Supply of nutrients to cells in engineered tissues, Biotechnol. Genet. Eng. Rev. 26 (2010) 163–178, 10.5661/bger-26-163.

[22]. Dunn JCY, Chan W-Y, Cristini V, Kim JS, Lowengrub J, Singh S, et al. , Analysis of cell growth in three-dimensional scaffolds, Tissue Eng. 12 (2006) 705–716, 10.1089/ten.2006.12.705. [PubMed: 16674285]

[23]. Lutzweiler G, Ndreu Halili A, Engin Vrana N, The overview of porous, bioactive scaffolds as instructive biomaterials for tissue regeneration and their clinical translation, Pharmaceutics 12 (2020), 10.3390/pharmaceutics12070602.

[24]. Walthers CM, Nazemi AK, Patel SL, Wu BM, Dunn JCY, The effect of scaffold macroporosity on angiogenesis and cell survival in tissue-engineered smooth muscle, Biomaterials 35 (2014) 5129–5137, 10.1016/j.biomaterials.2014.03.025. [PubMed: 24695092]

[25]. Freyman TM, Yannas IV, Gibson LJ, Cellular materials as porous scaffolds for tissue engineering, Prog. Mater. Sci. 46 (2001) 273–282, 10.1016/S0079-6425(00)00018-9.

[26]. Hollister SJ, Porous scaffold design for tissue engineering, Nat. Mater. 4 (2005) 518–524, 10.1038/nmat1421. [PubMed: 16003400]

[27]. Liu J, Xu HHK, Zhou H, Weir MD, Chen Q, Trotman CA, Human umbilical cord stem cell encapsulation in novel macroporous and injectable fibrin for muscle tissue engineering, Acta Biomater. 9 (2013) 4688–4697, 10.1016/j.actbio.2012.08.009. [PubMed: 22902812]

[28]. Fan C, Wang D-A, Macroporous hydrogel scaffolds for three-dimensional cell culture and tissue engineering, Tissue Eng. B Rev. 23 (2017) 451–461, 10.1089/ten.TEB.2016.0465.

[29]. Panayi AC, Smit L, Hays N, Udeh K, Endo Y, Li B, et al. , A porous collagen-GAG scaffold promotes muscle regeneration following volumetric muscle loss injury, Wound Repair Regen. 28 (2020) 61–74, 10.1111/wrr.12768. [PubMed: 31603580]

[30]. Haas GJ, Dunn AJ, Marcinczyk M, Talovic M, Schwartz M, Scheidt R, et al. , Biomimetic sponges for regeneration of skeletal muscle following trauma, J. Biomed. Mater. Res. 107 (2019) 92–103, 10.1002/jbm.a.36535.

[31]. Smoak MM, Mikos AG, Advances in biomaterials for skeletal muscle engineering and obstacles still to overcome, Mater. Today Bio. 7 (2020), 100069, 10.1016/j.mtbio.2020.100069.

[32]. Behmer Hansen RA, Wang X, Kaw G, Pierre V, Senyo SE, Accounting for material changes in decellularized tissue with underutilized methodologies, BioMed Res. Int. 2021 (2021), 6696295, 10.1155/2021/6696295. [PubMed: 34159202]

[33]. Ungerleider JL, Johnson TD, Rao N, Christman KL, Fabrication and characterization of injectable hydrogels derived from decellularized skeletal and cardiac muscle, Methods 84 (2015) 53–59, 10.1016/j.ymeth.2015.03.024. [PubMed: 25843605]

[34]. Kim W, Lee H, Lee J, Atala A, Yoo JJ, Lee SJ, et al. , Efficient myotube formation in 3D bioprinted tissue construct by biochemical and topographical cues, Biomaterials 230 (2020), 119632, 10.1016/j.biomaterials.2019.119632. [PubMed: 31761486]

[35]. Nichol JW, Koshy ST, Bae H, Hwang CM, Yamanlar S, Khademhosseini A, Cell-laden microengineered gelatin methacrylate hydrogels, Biomaterials 31 (2010) 5536–5544, 10.1016/j.biomaterials.2010.03.064. [PubMed: 20417964]

[36]. Yang J, Zhou M, Li W, Lin F, Shan G, Preparation and evaluation of sustained release platelet-rich plasma-loaded gelatin microspheres using an emulsion method, ACS Omega 5 (2020) 27113–27118, 10.1021/acsomega.0c02543. [PubMed: 33134671]

[37]. Liu L, Cheung TH, Charville GW, Rando TA, Isolation of skeletal muscle stem cells by fluorescence-activated cell sorting, Nat. Protoc. 10 (2015) 1612–1624, 10.1038/nprot.2015.110. [PubMed: 26401916]

[38]. Gerlinger-Romero F, Addinsall AB, Lovering RM, Foletta VC, van der Poel C, Della-Gatta PA, et al. , Non-invasive assessment of dorsiflexor muscle function in mice, J. Vis. Exp. (2019), 10.3791/58696.

[39]. Mintz EL, Passipieri JA, Lovell DY, Christ GJ, Applications of in vivo functional testing of the rat tibialis anterior for evaluating tissue engineered skeletal muscle repair, J. Vis. Exp. (2016), 10.3791/54487.

[40]. Draghi L, Resta S, Pirozzolo MG, Tanzi MC, Microspheres leaching for scaffold porosity control, J. Mater. Sci. Mater. Med. 16 (2005) 1093–1097, 10.1007/s10856-005-4711-x. [PubMed: 16362206]

[41]. Aguilar CA, Greising SM, Watts A, Goldman SM, Peragallo C, Zook C, et al. , Multiscale analysis of a regenerative therapy for treatment of volumetric muscle loss injury, Cell Death Dis. 4 (2018) 33, 10.1038/s41420-018-0027-8.

[42]. Wynn TA, Vannella KM, Macrophages in tissue repair, regeneration, and fibrosis, Immunity 44 (2016) 450–462, 10.1016/j.immuni.2016.02.015. [PubMed: 26982353]

[43]. Wosczyna MN, Rando TA, A muscle stem cell support group: coordinated cellular responses in muscle regeneration, Dev. Cell 46 (2018) 135–143, 10.1016/j.devcel.2018.06.018. [PubMed: 30016618]

[44]. Charles JP, Cappellari O, Hutchinson JR, A dynamic simulation of musculoskeletal function in the mouse hindlimb during trotting locomotion, Front. Bioeng. Biotechnol. 6 (2018) 61, 10.3389/fbioe.2018.00061. [PubMed: 29868576]

[45]. Braga TT, Agudelo JSH, Camara NOS, Macrophages during the fibrotic process: M2 as friend and foe, Front. Immunol. 6 (2015) 602, 10.3389/fimmu.2015.00602. [PubMed: 26635814]

[46]. Karande TS, Ong JL, Agrawal CM, Diffusion in musculoskeletal tissue engineering scaffolds: design issues related to porosity, permeability, architecture, and nutrient mixing, Ann. Biomed. Eng. 32 (2004) 1728–1743, 10.1007/s10439-004-7825-2. [PubMed: 15675684]

[47]. Dew L, MacNeil S, Chong CK, Vascularization strategies for tissue engineers, Regen. Med. 10 (2015) 211–224, 10.2217/rme.14.83. [PubMed: 25835483]

[48]. Khorshidi S, Solouk A, Mirzadeh H, Mazinani S, Lagaron JM, Sharifi S, et al. , A review of key challenges of electrospun scaffolds for tissue-engineering applications, J. Tissue Eng. Regen. Med. 10 (2016) 715–738, 10.1002/term.1978. [PubMed: 25619820]

[49]. Blake C, Massey O, Boyd-Moss M, Firipis K, Rifai A, Franks S, et al. , Replace and repair: biomimetic bioprinting for effective muscle engineering, APL Bioeng. 5 (2021), 031502, 10.1063/5.0040764. [PubMed: 34258499]

[50]. Kim JH, Seol Y-J, Ko IK, Kang H-W, Lee YK, Yoo JJ, et al. , 3D bioprinted human skeletal muscle constructs for muscle function restoration, Sci. Rep. 8 (2018), 12307, 10.1038/s41598-018-29968-5. [PubMed: 30120282]

[51]. Kang H-W, Lee SJ, Ko IK, Kengla C, Yoo JJ, Atala A, A 3D bioprinting system to produce human-scale tissue constructs with structural integrity, Nat. Biotechnol. 34 (2016) 312–319, 10.1038/nbt.3413. [PubMed: 26878319]

[52]. Seymour AJ, Shin S, Heilshorn SC, 3D printing of microgel scaffolds with tunable void fraction to promote cell infiltration, Adv. Healthc. Mater. 10 (2021), e2100644, 10.1002/adhm.202100644. [PubMed: 34342179]

[53]. Jana S, Levengood SKL, Zhang M, Anisotropic materials for skeletal-muscle-tissue engineering, Adv. Mater. Weinheim 28 (2016) 10588–10612, 10.1002/adma.201600240.

[54]. Veiseh O, Doloff JC, Ma M, Vegas AJ, Tam HH, Bader AR, et al. , Size- and shape-dependent foreign body immune response to materials implanted in rodents and non-human primates, Nat. Mater. 14 (2015) 643–651, 10.1038/nmat4290. [PubMed: 25985456]

[55]. Sussman EM, Halpin MC, Muster J, Moon RT, Ratner BD, Porous implants modulate healing and induce shifts in local macrophage polarization in the foreign body reaction, Ann. Biomed. Eng. 42 (2014) 1508–1516, 10.1007/s10439-013-0933-0. [PubMed: 24248559]

[56]. Xia P, Luo Y, Vascularization in tissue engineering: the architecture cues of pores in scaffolds, J. Biomed. Mater. Res. Part B Appl Biomater 110 (2022) 1206–1214, 10.1002/jbm.b.34979.

[57]. Jones AC, Arns CH, Hutmacher DW, Milthorpe BK, Sheppard AP, Knackstedt MA, The correlation of pore morphology, interconnectivity and physical properties of 3D ceramic scaffolds with bone ingrowth, Biomaterials 30 (2009) 1440–1451, 10.1016/j.biomaterials.2008.10.056. [PubMed: 19091398]

[58]. Murphy SV, Atala A, 3D bioprinting of tissues and organs, Nat. Biotechnol. 32 (2014) 773–785, 10.1038/nbt.2958. [PubMed: 25093879]

[59]. Choi Y-J, Jun Y-J, Kim DY, Yi H-G, Chae S-H, Kang J, et al. , A 3D cell printed muscle construct with tissue-derived bioink for the treatment of volumetric muscle loss, Biomaterials 206 (2019) 160–169, 10.1016/j.biomaterials.2019.03.036. [PubMed: 30939408]

[60]. Quarta M, Cromie Lear MJ, Blonigan J, Paine P, Chacon R, Rando TA, Biomechanics show stem cell necessity for effective treatment of volumetric muscle loss using bioengineered constructs, Npj Regen. Med. 3 (2018) 18, 10.1038/s41536-018-0057-0. [PubMed: 30323949]

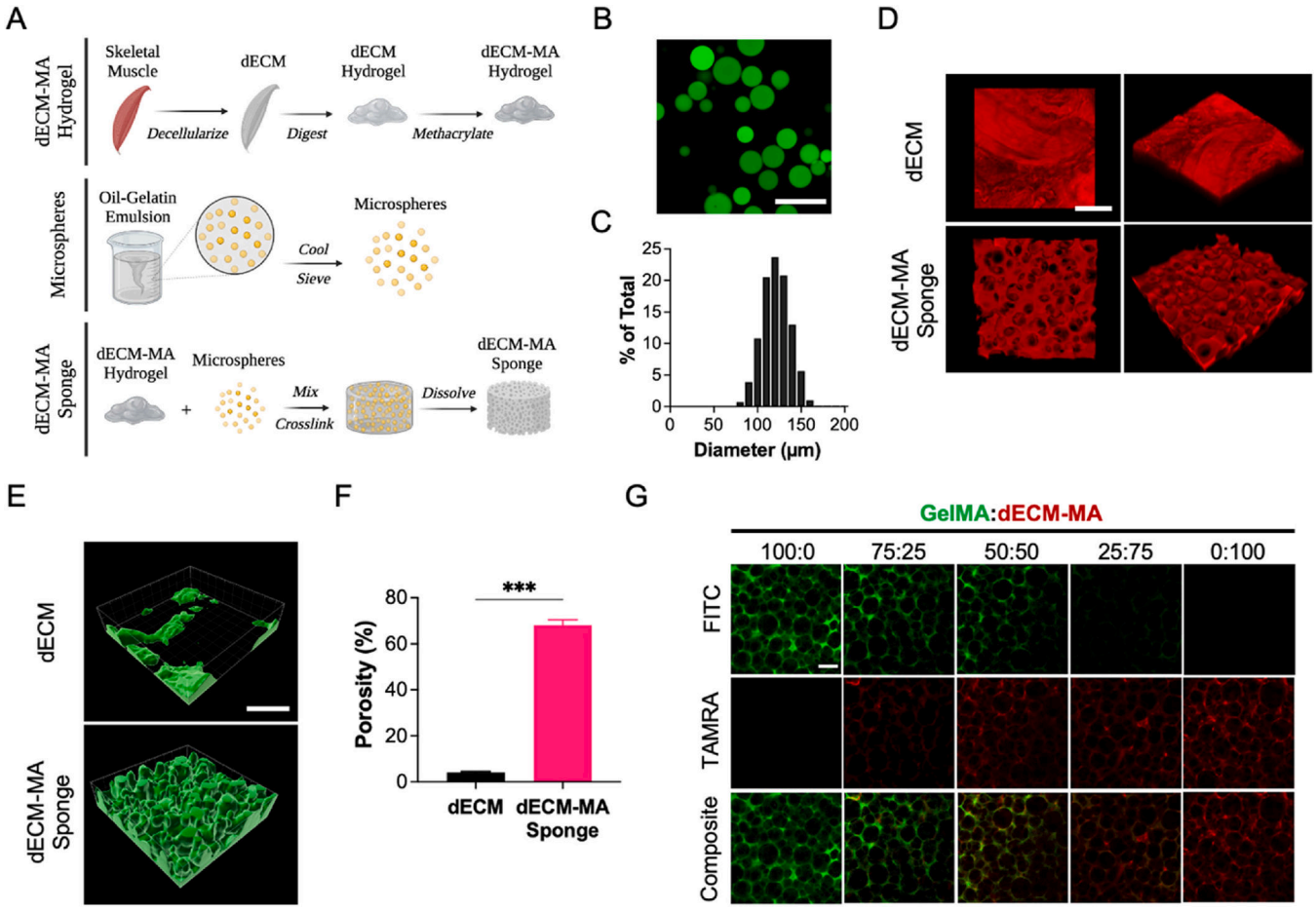

Fig. 1.

Fabrication and characterization of macroporous dECM-MA sponge scaffolds. (**A**) Schematic of dECM-MA hydrogel, gelatin microsphere, and dECM-MA sponge synthesis. (**B**) Confocal microscopy of fluorescently labeled gelatin microspheres. (**C**) Histogram of gelatin microsphere size distribution. (**D**) 3D IMARIS rendering of fluorescently labeled dECM and dECM-MA sponge scaffolds. (**E**) 3D IMARIS rendering of void space volume, visualized within scaffolds using high molecular weight FITC-dextran to fill pores. (**F**) Quantification of porosity, or void space fraction, calculated from IMARIS renderings (n = 4). *** = $P < 0.0001$. (**G**) Confocal microscopy images of dECM-MA/GelMA hybrid sponge scaffolds. GelMA and dECM-MA hydrogel precursors were fluorescently labeled with FITC and TAMRA, respectively. All scale bars = 150 μm.

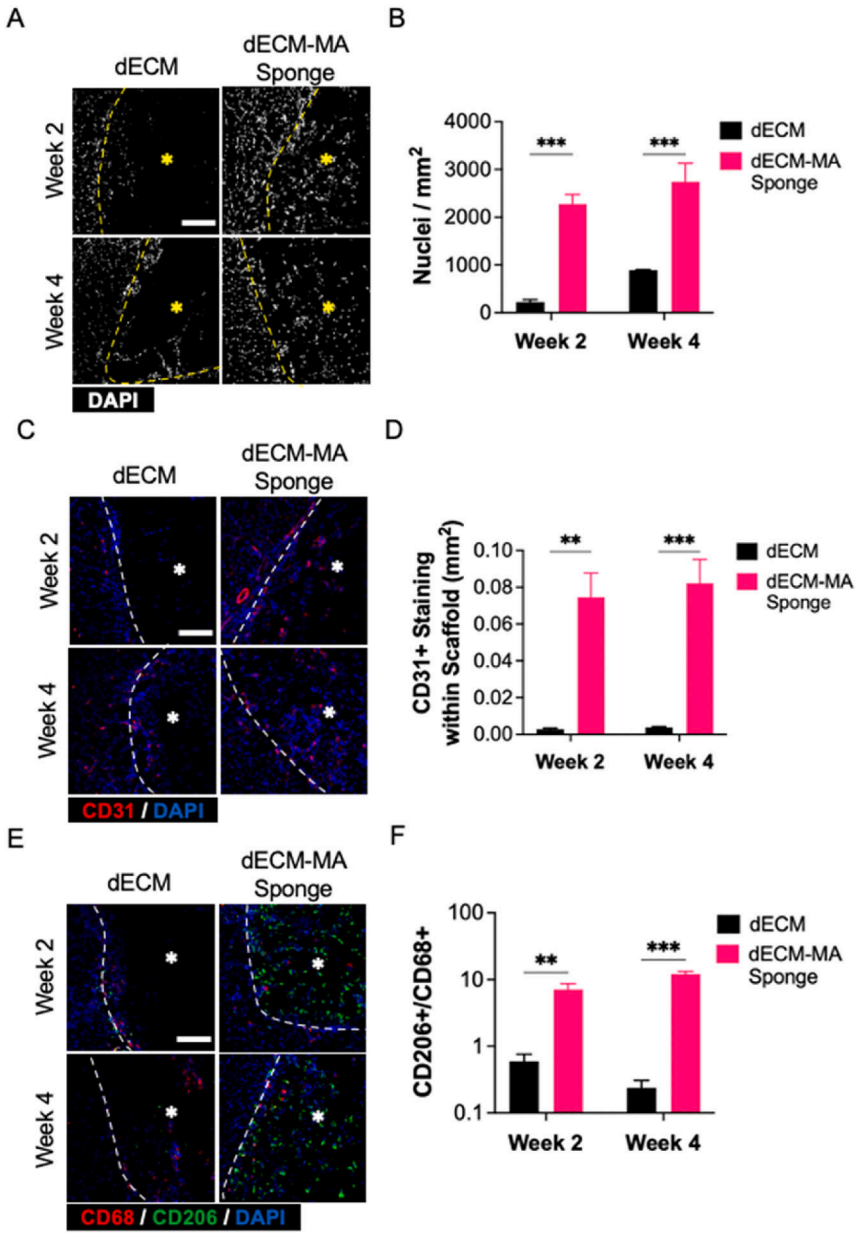

Fig. 2.

Acellular dECM-MA sponges promote early cellularization, endothelialization, and establishment of a pro-regenerative immune microenvironment in a mouse VML model. (**A**) DAPI staining of TA cross-sections showing cell infiltration within scaffolds. (**B**) Quantification of DAPI density (# of nuclei/scaffold area) within scaffolds (n = 4). (**C**) Immunofluorescence (IF) images of TA cross-sections. (**D**) Quantification of $CD31^{+}$ staining within scaffolds (n = 4). (**E**) IF images of TA cross-sections (n = 4). (**F**) Calculated M2/M1 macrophage ratios (# CD206+ cells/# $CD68^{+}$ cells) within scaffolds. ** = $P < 0.001$; *** = $P < 0.0001$. Scaffolds denoted with an asterisk (*) and scaffold-muscle interfaces indicated by dashed lines. All scale bars = 150 μm.

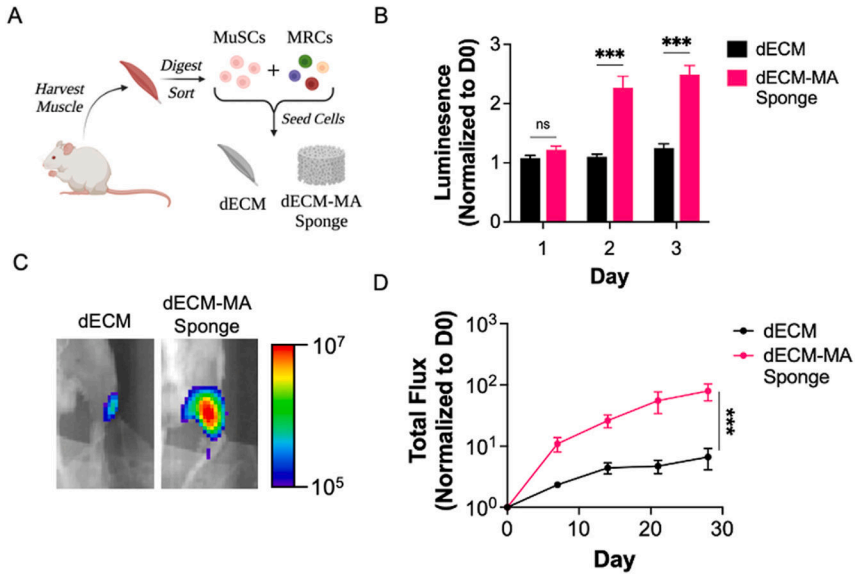

Fig. 3.

Macroporous dECM-MA sponges enhance proliferation of primary MuSCs *in vitro* and *in vivo*. (**A**) Schematic of bioconstruct preparation. Hindlimb muscles from donor mice were digested and sorted to isolate MuSC (Luc+) and MRC (Luc−) cell populations. Cells were mixed at a defined ratio (described in Methods) and seeded onto dECM and dECM-MA sponge scaffolds. (**B**) Quantified results of *in vitro* bioluminescence generated from cultured bioconstructs. Bioluminescence was measured daily for three days (n = 3). (**C**) Representative images of bioluminescence signals 28 days after implantation, generated from bioconstructs implanted in TA muscles immediately following VML injury. (**D**) Quantification of *in vivo* bioluminescence imaging over 28 days (n = 4). *** = $P < 0.0001$.

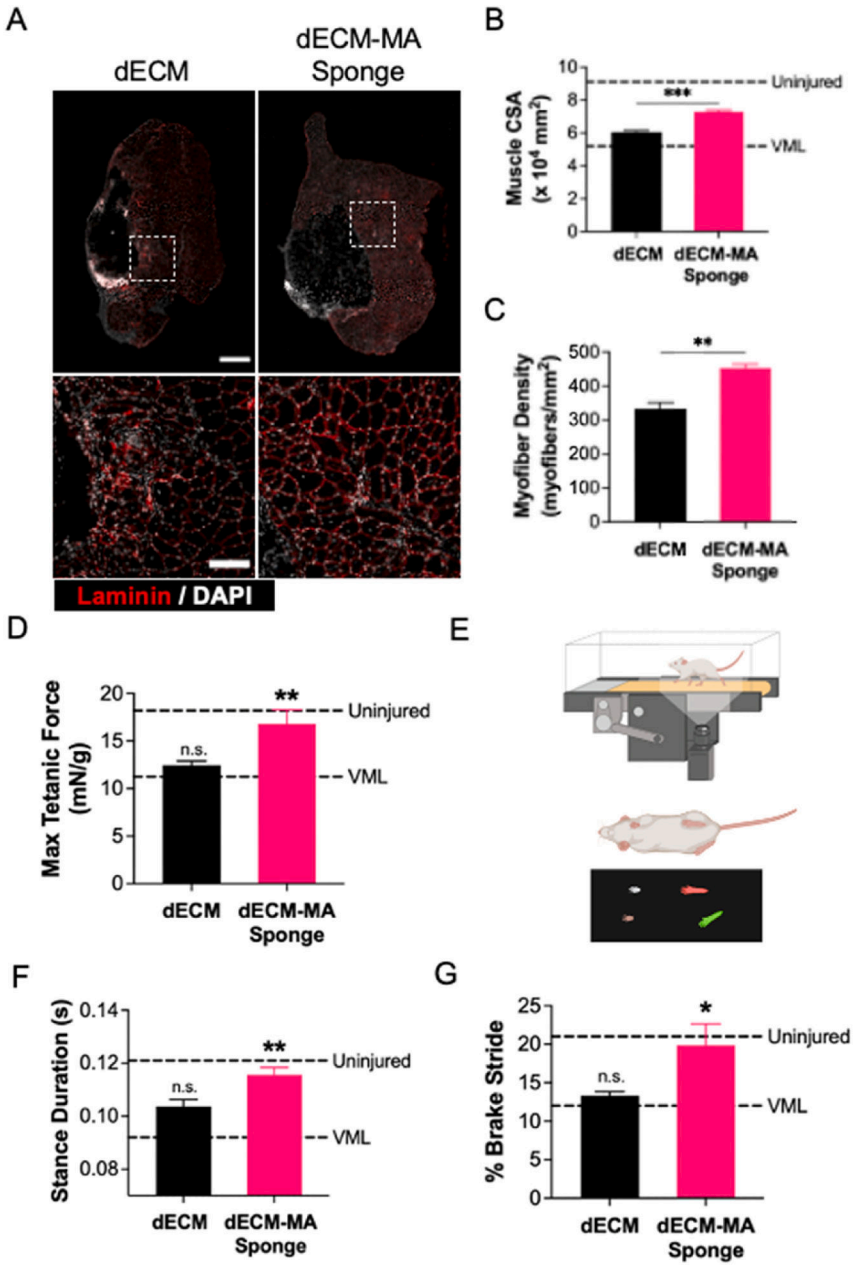

Fig. 4.

Macroporous dECM-MA sponges improve muscle regeneration and functional recovery in a mouse VML model. (**A**) Representative IF images of TA cross sections (top, scale bar = 500 μm) and higher magnification of areas containing regenerating myofibers (bottom, scale bar = 150 μm). (**B**) Quantification of muscle cross-sectional area (CSA) (n = 4). (**C**) Quantification of regenerating myofiber density (# of myofibers/field of view) from TA cross sections (n = 4). (**D**) Measurements of *in vivo* force production, normalized by bodyweight, of TA muscles treated with bioconstructs following VML injury (n = 4). Dashed lines represent the normalized average force production of uninjured and untreated VML controls (n = 4). (**E**) Schematic of DigiGait treadmill system (top) and individual paw

labels for gait analysis (bottom). (**F, G**) Quantification of (F) stance duration and (G) percent brake stride, the percent of time during each stride that the paw is in the braking phase, four weeks after bioconstruct implantation (n = 4). * = $P < 0.05$; ** = $P < 0.001$; *** = $P < 0.0001$.

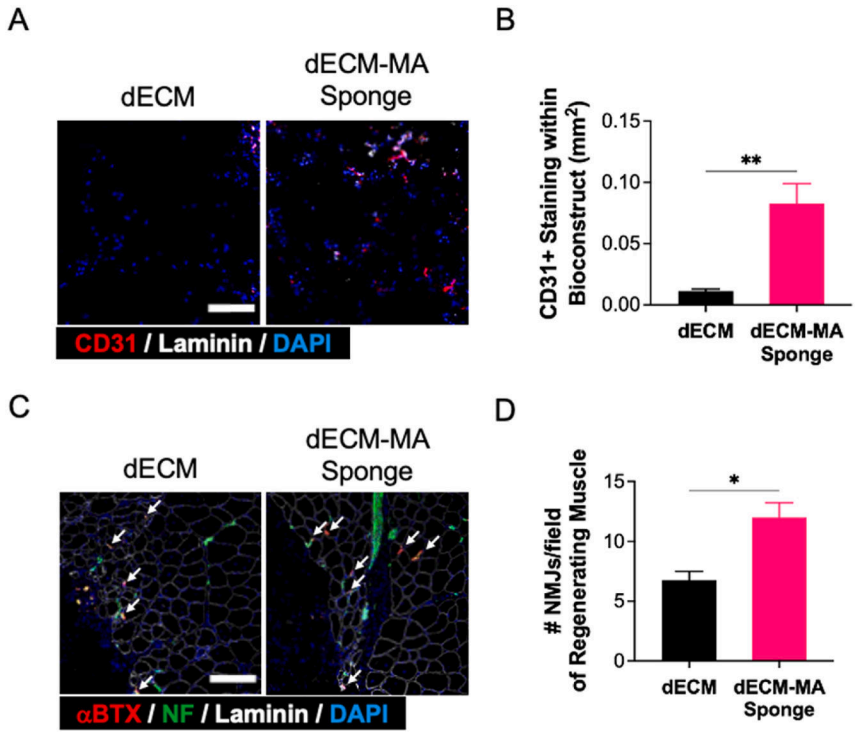

Fig. 5.

Macroporous dECM-MA sponges enhance bioconstruct endothelialization and innervation of regenerated muscle. (**A**) Representative IF images within bioconstruct and at muscle-bioconstruct interface in cross-sections of TAs treated with dECM and dECM-MA sponge bioconstructs four weeks after implantation. (**B**) Quantification of $CD31^{+}$ staining within remaining bioconstruct (n = 4). (**C**) Representative IF images of TA cross-sections. White arrows indicate neuromuscular junctions (NMJs). (**D**) Quantification of NMJs within areas of regenerating muscle fibers (n = 4). * = $P < 0.05$; ** = $P < 0.001$; Scale Bars = 150 μm.

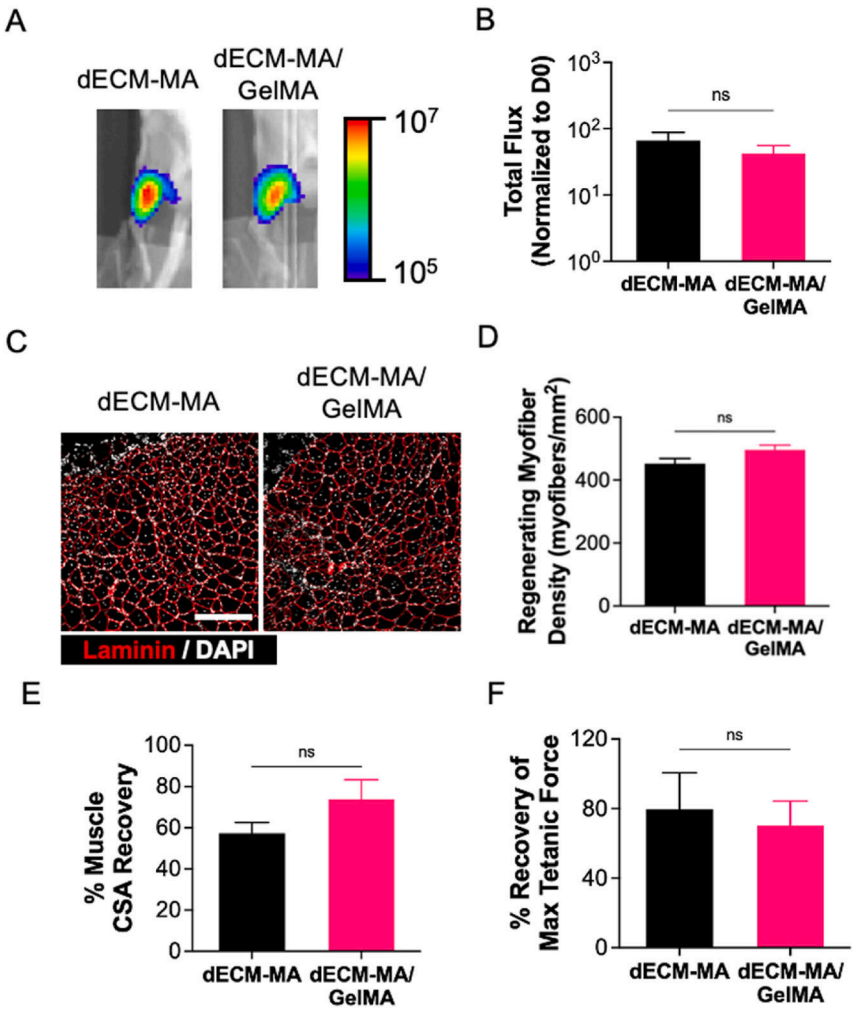

Fig. 6.

Hybrid dECM-MA/GelMA sponges (50/50 ratio) improve MuSC transplantation and muscle regeneration following VML comparably to dECM-MA sponges. (**A**) Representative images of bioluminescence signals 28 days after dECM-MA and dECM-MA/GelMA bioconstruct implantation. (**B**) Quantification of *in vivo* bioluminescence imaging on day 28 (n = 4). (**C**) Representative IF images of regenerating muscle four weeks post-implantation of dECM-MA and dECM-MA/GelMA bioconstructs (scale bar = 250 μm). (**D**) Quantification of regenerating myofiber density from TA cross sections (n = 4). (**E**) Quantification of percent muscle cross-sectional area (CSA) recovery (n = 4). (**F**) Quantification of percent recovery of *in vivo* force production (n = 4).

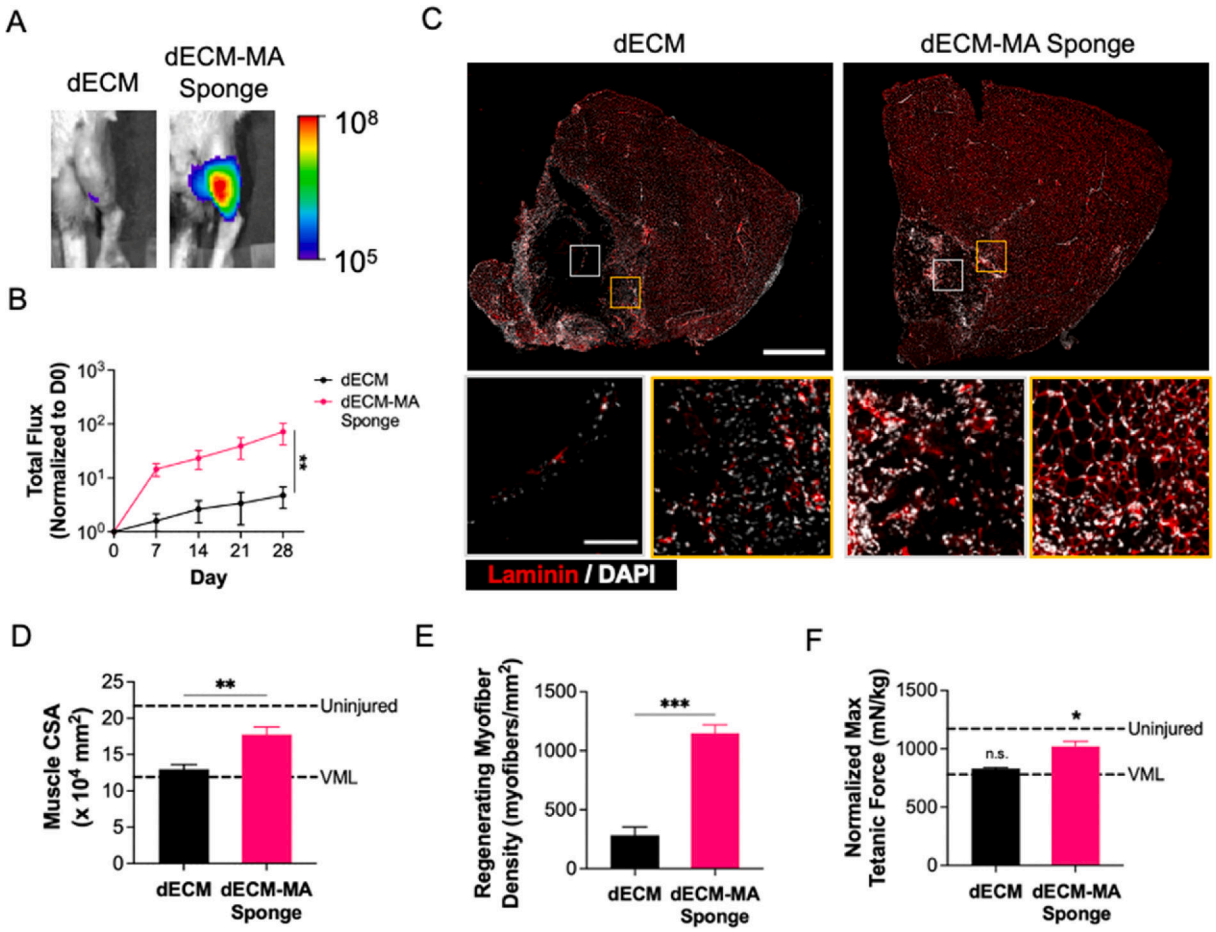

Fig. 7.

Macroporous dECM-MA sponge bioconstructs improve muscle regeneration and functional recovery in a rat VML model. (**A**) Representative images of bioluminescence signals 28 days after bioconstruct implantation. (**B**) Quantification of *in vivo* bioluminescence imaging over 28 days (n = 4). (**C**) Representative IF images of TA cross sections (top, scale bar = 1 mm) and higher magnification images (bottom, scale bar = 150 μm) of areas containing regenerating myofibers within bioconstructs (white outline) and at the bioconstruct-muscle interface (orange outline). (**D**) Quantification of muscle cross-sectional area (n = 4). (**E**) Quantification of regenerating myofiber density from TA cross sections (n = 4). (**F**) Measurement of *in vivo* force production, normalized by bodyweight, of TA muscles treated with each bioconstruct 28 days after implantation (n = 4). * = $P < 0.05$; ** = $P < 0.001$; *** = $P < 0.0001$. (For interpretation of the references to colour in this figure legend, the reader is referred to the Web version of this article.)